Signal Processing 202 (2023) 108774

Contents lists available at ScienceDirect

Signal Processing

journal homepage: www.elsevier.com/locate/sigpro

Ghosting-free multi-exposure image fusion for static and dynamic scenes

Oguzhan Ulucan, Diclehan Ulucan, Mehmet Turkan*

Department of Electrical and Electronics Engineering, Izmir University of Economics, Izmir, Turkey

ARTICLE INFO

Article history:
Received 22 February 2022
Revised 22 August 2022
Accepted 4 September 2022
Available online 12 September 2022

Keywords:
High dynamic range
Multi-exposure image fusion
Principal component analysis
Saliency map
Well-exposedness

ABSTRACT

The visual system enables humans to perceive all details of the real-world with vivid colors, while high dynamic range (HDR) technology aims at capturing natural scenes in a closer way to human perception through a large dynamic range of color gamut. Especially for traditional –low dynamic range (LDR)– devices, HDR-like image generation is an attractive research topic. Blending a stack of input LDR exposures is called multi-exposure image fusion (MEF). MEF is indeed a very challenging problem and it is highly prone to halo effects or ghosting and motion blur in the cases when there are spatial discontinuities in between input exposures. To overcome these artifacts, MEF keeps the "best" quality regions of each exposure via a weight characterization scheme. This paper proposes an effective weight map extraction framework which relies on principal component analysis, adaptive well-exposedness and saliency maps. The characterized maps are later refined by a guided filter and a blended output image is obtained via pyramidal decomposition. Comprehensive experiments and comparisons demonstrate that the developed algorithm generates very strong statistical and visual results for both static and dynamic scenes. In addition, the designed method is successfully applied to the visible-infrared image fusion problem without any further optimization.

1. Introduction

The human visual system (HVS) can perceive thousands of colors and fine details present in natural scenes. On the other hand, artificial vision systems which are developed based on the HVS may have critical drawbacks. For instance, HDR compatible cameras and screens can be used to capture and display high contrast natural scenes in a closer way to human observers. However, HDR equipment has still a relative high-cost, hence it may currently be not affordable for many consumers. In order to lower the economic burden, HDR cameras can be used to capture HDR content which can then be mapped to conventional LDR screens via tone-mapping operators. Yet, tone-mapping may produce undesired outcomes such as low-subjective contrast and color saturation [1,2]. Alternatively, one can prefer to obtain high-quality LDR (HDR-like) images through MEF approaches [3], which is not only useful in HDR imaging but also in applications such as haze removal [4,5].

MEF aims at keeping the "best parts" of each distinct exposure while blending an input stack into a single informative image [6]. The fusion operation is guided by weight maps which highlight the most detailed and informative parts of each LDR exposure. The map extraction process is troublesome for both static and dynamic scenes, and the faulty computed weights may cause undesired sharp color changeovers, jitter effects, halos and ghosting artifacts [3]. Therefore, the main objective is to develop robust weight map extraction and/or characterization methods which will be consequently the novel parts of MEF techniques. To this end, this study introduces a novel MEF algorithm to fuse both static and dynamic scenes. The weight map characterization process relies on principal component analysis (PCA), adaptive well-exposedness and saliency map features. These weights are subsequently refined by a guided filter and the fusion stage is conducted via pyramidal decomposition. Note that an additional image alignment step is performed via histogram matching for dynamic contents.

To the best of available knowledge, it is the first time that PCA is employed in this study to characterize weight maps in MEF. Furthermore, well-exposedness, which is related to brightness, is modified to be fully adaptive, while existing MEF algorithms adopt a fixed parameter and/or constant for this feature. It is also important to note here that saliency maps are utilized in this study to mimic the HVS, to assign larger weights to the most informative parts of input exposures as in the primary visual cortex. The proposed MEF technique, henceforth referred to as PAS-MEF, is compared against several state-of-the-art methods and it presents strong statistical and visual outputs, while outperforming most of

* Corresponding author.
E-mail address: mehmet.turkan@iue.edu.tr (M. Turkan).

https://doi.org/10.1016/j.sigpro.2022.108774
0165-1684/

the well-known MEF algorithms. Additionally, PAS-MEF is successfully applied to solve the visible-infrared image fusion problem which further demonstrates its general usability and effectiveness.

This paper is organized as follows. The related work from the literature is presented in Section 2. The proposed MEF technique is explained in Section 3. Experimental setup is detailed and results are discussed for both MEF and visible-infrared fusion in Section 4. Lastly, a brief summary of this study and possible future directions are provided in Section 5.

2. Related work

A milestone MEF method is proposed by Mertens et al. [6]. In this pixel-based approach, contrast, saturation and well-exposedness features are extracted and employed as fusion maps. The fused output is then obtained through Gaussian pyramid of weight maps and Laplacian pyramid of input exposures. This method is designed only for static image stacks and it provides satisfying results both visually and statistically. In the study of Hu et al. [7], an image alignment approach is developed to solve the ghosting problem in MEF. For a given input stack, the most well-exposed exposure is selected as the reference image. A latent image is then formed for each of the remaining exposures, which structurally looks like the reference but is exposed like the source. The obtained new stack is finally fused similar to Mertens et al. [6]. A successful image fusion algorithm is presented by Li et al. [8]. The algorithm is based on two-scale image decomposition in which fusion is done in two different scales, namely base- and detail-layer. The fusion is controlled with guided filtering-based weighted average technique. This method produces state-of-the-art results for not only MEF purposes, but also multi-spectral, multi-focus, multi-modal fusion applications. Another MEF algorithm, which depends on ghosting removal and selective detail enhancement, is introduced by Li et al. [9]. A bidirectional normalization-based method is used to detect inconsistent pixels, while a two-round hybrid technique is employed to correct these inconsistencies. Moreover, a content adaptive bilateral filter is adopted to extract the fine details in the gradient domain. An intermediate image is then reconstructed via a multi-scale fusion of all corrected images. Lastly, the selected fine details are added to this blended image. In the study of Qin et al. [10], an iterative patch-based method, which relies on geometry and color information, is developed to match and find corresponding image patches in different input exposures containing moving objects. In order to preserve these objects in the output, corresponding patches are simultaneously fused via the random walker algorithm in accordance with the match and find procedure. An approach for both static MEF and multi-focus image fusion is introduced by Paul et al. [11]. This algorithm operates in the YCbCr color space and the fusion operation is performed for luminance and chrominance channels independently. The luminance channels are blended through a wavelet-based fusion technique in the gradient domain, while the blending of chrominance channels is carried out by taking a weighted sum of chrominance values. In Nejati et al. [12], a method based on two-scale image decomposition is proposed to fuse static image sequences. For the base and detail layers of the luminance components of input exposures, the exposedness features are extracted to form weight maps. Afterwards, a weighted averaging is applied to the base and detail layers separately. These two fusion results are finally combined to obtain the blended output image. In another successful MEF algorithm proposed by Kou et al. [13], multi-scale image fusion is carried by an edge preserving smoothing pyramid in order to obtain more information from highlights and shadows, while preserving the texture information in sequences. The method produces high quality output images both qualitatively and quantitatively. In a recent study, a patch-based MEF for both static and dynamic scenes is designed by Ma et al. [14]. The fusion weights are formed by computing signal strength, signal structure and mean intensity. This algorithm outperforms several state-of-the-art methods and it produces very slight ghosting artifacts for dynamic scenes. In Li et al. [15], this study is later modified with recursive down-sampling and processing, which results in successfully reduced halo effects and execution times. An adaptive weight extraction scheme for static MEF is proposed by Lee et al. [16]. Two different weight maps are extracted as follows: the gradient information of each exposure is used to form the first map and an adaptive version of well-exposedness in Mertens et al. [6] is employed to characterize the second map. The fusion is performed via pyramidal image decomposition. Yet a MEF technique for both static and dynamic scenes is developed by Hayat and Imran [17]. Three distinct weight maps, namely, local contrast, brightness and color dissimilarity, are employed in this study. Histogram equalization and median filtering are used to obtain the color dissimilarity, while the dense-SIFT descriptor is adopted to compute the local contrast feature. A guided filter is employed to eliminate noise and discontinuities in these maps, and then the fusion is carried out via pyramidal image decomposition. A very recent method based on neural networks, so called GANFuse to preserve and fuse the informative parts of extreme exposure pairs (i.e., under- and over-exposed) is proposed by Yang et al. [18]. GANFuse is a generative adversarial networks-based static MEF scheme relying on the increasing number of discriminators of FusionGAN [19] which is designed for the fusion of visible and infrared images. GANFuse operates in the luminance channel only, while a weighted fusion is carried out for chrominance channels independently. A recent multi-exposure image fusion study proposed by Qi et al. [20] is designed especially for the dynamic cases to overcome the ambiguities in fused images for dynamic cases. The ghosting-free algorithm relies on the feature patches and guided filter decomposition for robust fusion. In another recent work, a static MEF approach based on linear embeddings and watershed masking is introduced by Ulucan et al. [3]. While the local geometry of the image manifold structure is preserved successfully, linear embeddings of exposure image patch spaces are used to form weight maps. In order to highlight and preserve the most informative parts of each input exposure, these weight maps are then refined via watershed masking. The fusion is finally performed via weighted averaging.

3. The proposed method of exposure fusion

This study develops a novel MEF framework which is based on PCA, adaptive well-exposedness and saliency features for weight map characterization. Each of these individual maps presents its effectiveness by covering diverse information present in the input stack. The proposed PAS-MEF scheme is illustrated in a simple flowchart in Fig. 1. While the main algorithm begins to process input images with the weight map characterization block, an additional branch leading to image alignment is followed in the case of dynamic sequences. After all maps are extracted, the fused HDR-like output is obtained via pyramidal decomposition. In the remainder of this section, the PAS-MEF algorithm is explained in details.

3.1. Image alignment via histogram matching

MEF algorithms generate HDR-like outputs from a set of LDR inputs. These methods can produce precise outputs for the input exposures which are perfectly aligned. However, in practice, there is no guarantee that all exposures in the bracket are well-aligned. Therefore, one of the biggest challenges in MEF is to remove the motion blur or ghosting artifacts when there is local or global motion in between input exposures [3].

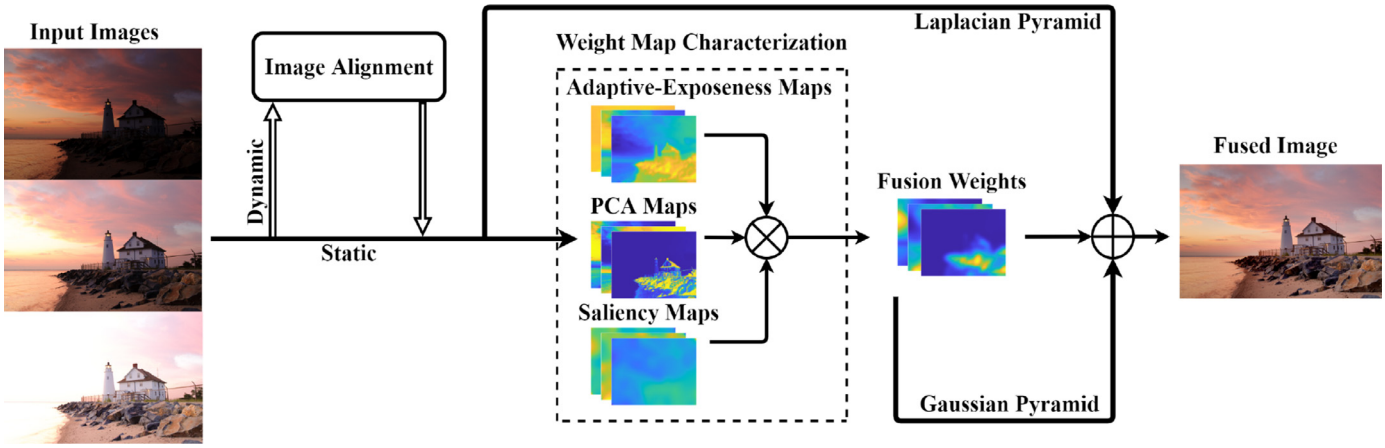

Fig. 1. Flowchart of PAS-MEF.

Fig. 2. (Top) Input exposures and (bottom) aligned outputs.

The presence of motion is considered to disturb the photometric relation between pixels in the region of movement when MEF operates in the spatial domain [21]. A common technique to overcome this problem is to employ image alignment methods. In these approaches, a reference input image is determined and the intensities of other input exposures are mapped onto those of reference image. Consequently, dynamic scenes are transformed into static images, thus can be processed without any further consideration of motion.

In PAS-MEF, image alignment is used as a pre-processing technique for dynamic image sequences. For N exposures I_n in the input stack, the median image is selected as the reference I_{ref} and the histograms of the remaining $(N-1)$ inputs are matched to this reference image as given in Eq. (1),

$$I_n \leftarrow \texttt{HistMatch}(I_n, I_{ref}), \quad n = 1 \dots N, \tag{1}$$

where `HistMatch` denotes the *histogram matching* operator. A simple example dynamic scene with three input exposures and the image alignment results are illustrated in Fig. 2.

3.2. Weight map characterization

3.2.1. Weight maps via PCA

PCA reduces the dimensionality of large datasets by exploiting the underlying correlation between variables, while preserving most of the information efficiently. In order to obtain uncorrelated variables from possibly correlated data, PCA carries out an orthogonal transformation [22]. The eigenvectors of the covariance matrix are employed to project the correlated data onto PCA space. The representations of data in this space can be called as *scores*. To the best of available knowledge, PCA has not been utilized in MEF studies, whereas it has already been adopted in the field of image fusion [23].

In this study, PCA scores are extracted and employed as weight maps. Firstly, gray-scale versions of input images I_n, $n = 1 \dots N$, are vectorized into column vectors of the size $(rc \times 1)$ where r and c are the number of rows and columns of each exposure, respectively. In order to compute the scores, all these column vectors are used to form an $(rc \times N)$ data matrix consisting of rc observations with N variables each. After calculating PCA scores of all observations, each variable-score vector is linearly normalized to the range [0,1] and this data is reshaped back to an $(r \times c)$ matrix per exposure. These normalized-score matrices are then processed by a Gaussian filter to eliminate possible noise and discontinuities, while smoothing the sharp changeovers at transition regions. Lastly, a sum-to-one normalization is performed at each spatial position (r, c) over all exposures and the final PCA weight map P_n, $n = 1 \dots N$, is obtained to be used in the fusion process. In Fig. 3 (top-row), the obtained P_n are exemplified for the *Lighthouse* stack.

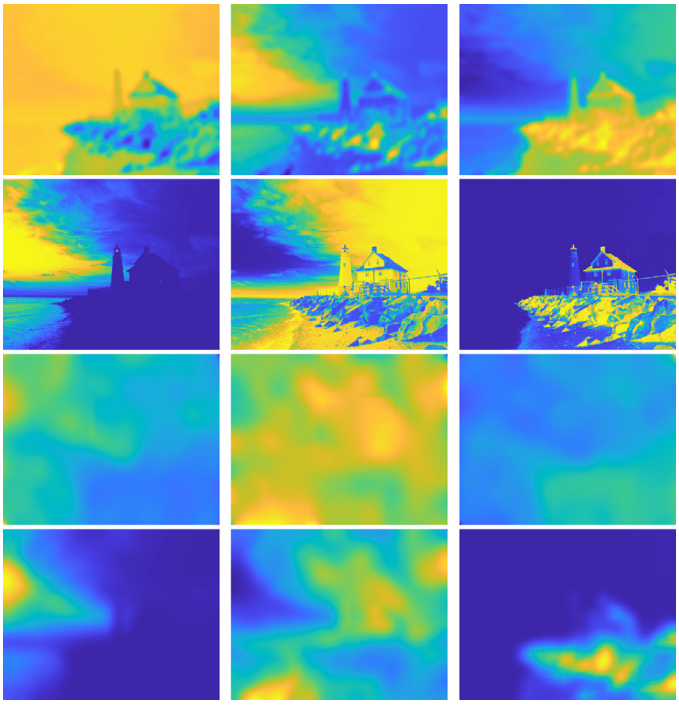

Fig. 3. (Top-row) PCA (P_n), (second-row) adaptive well-exposedness (A_n), (third-row) saliency (S_n) and (bottom-row) final fusion (W_n) maps for the *Lighthouse* stack. (Left-to-right) Under-exposure, normal-exposure, over-exposure. $n = 1, 2, 3$.

3.2.2. Weight maps via adaptive well-exposedness

The well-exposedness feature is initially derived in Mertens et al. [6] in order to preserve the well-settled regions in the input stack, i.e., to neglect under- and over-exposed pixel intensities. It is extracted from each normalized exposure I_n via a Gaussian curve, such that $exp\big(-(I_n - 0.5)^2/2\sigma^2\big)$ where $\sigma = 0.2$. This weight intends to keep pixels which are not too close to 0 or 1. In other words, it aims at preserving well-exposed pixels having intensity values close to 0.5. However, the preservation of bright regions of short-exposure images and dark regions of long-exposure images might be troublesome with this formulation. Hence, areas containing significant information can be missed, which will negatively impact the quality of the fused output. To provide a solution to this problem, an adaptive well-exposedness feature is developed in Lee et al. [16]. This scheme is based on the mean of pixel intensities of neighboring exposures I_{n-1} and I_{n+1} of I_n, in order to remove the constant parameters 0.5 and σ in Mertens et al. [6]. Nevertheless, the adaptive formulation here still requires a fixed parameter to compute σ.

In this paper, a fully adaptive well-exposedness characterization is proposed to preserve bright areas in short-exposure images and dark areas in long-exposure images, as well as well-exposed areas in all exposures. The fully adaptive well-exposedness weight map A_n, $n = 1 \dots N$, is computed on the luminance channel Y_n of I_n as given in Eq. (2),

$$A_n = exp\big(-(Y_n - (1 - \mu_{Y_n}))^2/2\sigma_{Y_n}^2\big), \tag{2}$$

where μ_{Y_n} and σ_{Y_n} are the mean and the standard deviation of pixel intensities in Y_n, respectively. As a result, the Gaussian curve parameters are computed by means of the self-statistical information contained in each input, and larger weights will be assigned to the best luminance intensities of each individual exposure. In Fig. 3 (second-row), the calculated A_n are presented for the *Lighthouse* stack.

3.2.3. Weight maps via saliency

The visual sampling process of the HVS has been intensively studied to model its mechanism [24]. It is noticed that the attention an object gathers (via the HVS processing) relies on the task at hand and stimulus-driven factors such as prominent colors [24]. In order to mimic the HVS, numerous computational models are introduced aiming at highlighting salient regions. In image processing tasks, saliency maps [25] are widely used to increase the quality of images and present visually more appealing outputs.

In this study, salient image regions (which are more attractive to human observers) are assigned with larger weights through saliency maps. Since modeling a new saliency algorithm is out of context, the method of Hou et al. [26] is adopted into PAS-MEF. This method depends on the *image signature descriptor*, which is defined as the sign of the Discrete Cosine Transform (DCT) coefficients. In simple terms, the DCT of an input exposure is calculated and the inverse DCT of the sign of the DCT coefficients is computed to perform image reconstruction. The saliency weight map S_n, $n = 1 \dots N$, is then extracted from the reconstructed image. For more information, the reader may refer to Hou et al. [26]. In Fig. 3 (third-row), the obtained S_n are provided for the *Lighthouse* stack.

3.3. Weight map refinement and image fusion

After three different weight maps are extracted for each distinct image in the input stack, they are combined to form a single and refined map W_n per exposure as given in Eq. (3),

$$W_n = \texttt{GuidFilt}(P_n \times A_n \times S_n), \;\; n = 1 \dots N, \tag{3}$$

where `GuidFilt` represents the *guided filter* [27]. This filter is an edge-preserving smoothing operator which eliminates possible discontinuities and noise in the combined maps. The obtained maps W_n are finally normalized to satisfy a sum-to-one constraint at each spatial position (r, c) over all exposures in order to characterize the final fusion weight maps. In Fig. 3 (bottom-row), the calculated W_n are illustrated for the *Lighthouse* stack.

Since each input exposure has distinct local intensities, a direct weighted-blending strategy may produce artifacts and unsatisfactory outputs [6]. Therefore, a pyramidal fusion approach [6,28] is preferred to avoid halo effects at sharp texture and color changeovers. Each exposure image is decomposed into ℓ-levels of distinct resolutions via the Laplacian pyramid (L), while a similar process is performed for the final fusion weights through the Gaussian pyramid (G). Subsequently, the weighted blending procedure is applied at each pyramidal level to acquire a fused Laplacian pyramid for the fused image in Eq. (4) as follows,

$$L\{F^\ell\} = \sum_{n=1}^{N} G\{W_n^\ell\} \times L\{I_n^\ell\}, \tag{4}$$

where the fused pyramid $L\{F^\ell\}$ is finally collapsed to obtain the final output image F.

4. Experimental setup and results

The proposed PAS-MEF is compared with Mertens09 [6], Li13 [8], Paul16 [11], Nejati17 [12], Kou17 [13], Ma17 [14], Lee18 [16], Hayat19 [17], Li20 [15], Yang20 [18] and Ulucan21 [3] for static scenes, and it is compared against Hu13 [7], Li14 [9], Qin14 [10], Ma17, Hayat19, Li20 and Qi20 [20] for dynamic image stacks.

Detailed information about the used image datasets is provided in Tables 1 and 2 for static and dynamic stacks, respectively. Several of these test images are adopted from the studies in Ma et al. [29], Merianos and Mitianoudis [30], Fang et al. [31]. Further, *Izmir-Cordon* and *IzmirFair* are courtesy of Erdem Okur of Izmir Uni-

Table 1
Static image stacks used in the experiments.

Name	Size	Name	Size
Arno	339 × 512 × 3	*Lighthouse*	340 × 512 × 3
Chinese Garden	340 × 512 × 3	*Mask*	341 × 512 × 3
Church	512 × 335 × 3	*Office*	340 × 512 × 6
Farmhouse	341 × 512 × 3	*Oldhouse*	720 × 1080 × 3
Flowers	720 × 1080 × 3	*Ostrow*	341 × 512 × 3
IzmirCordon	518 × 690 × 3	*Set*	341 × 512 × 3
IzmirFair	456 × 342 × 3	*Tower*	512 × 341 × 3
Kluki	341 × 512 × 3	*Treeunil*	600 × 808 × 7
Landscape	341 × 512 × 3	*Venice*	341 × 512 × 3
Laurenziana	512 × 356 × 3	*Window*	384 × 512 × 3
YellowHall	339 × 512 × 3		

Table 2
Dynamic image stacks used in the experiments.

Name	Size	Name	Size
Arch	1024 × 669 × 5	*Puppets*	1024 × 812 × 5
Brunswick	683 × 1024 × 3	*Readingman*	2448 × 3264 × 3
Cliff	683 × 1024 × 3	*Russ1*	683 × 1024 × 3
Campus	648 × 1011 × 6	*SculptureGarden*	754 × 1024 × 5
Forest	683 × 1024 × 4	*Square*	683 × 1024 × 3
Horse	690 × 1024 × 3	*Tate3*	683 × 1024 × 3
Lady	3872 × 2592 × 3	*Wroclav*	683 × 1024 × 3
Llandudno	683 × 1024 × 3	*YWFusionopolis*	712 × 1072 × 6
ProfJeonEight	1424 × 2144 × 7		

versity of Economics. All comparison images are produced via either running the original implementations provided on the webpages of respective projects or respective authors themselves. All methods including PAS-MEF are employed in their default settings without any optimization. It is important to note that the experiments of Yang20 are conducted by its authors via a 2.4 GHz Intel Xeon CPU E5 – 2673 v3, GeForce GTX 2080Ti and 64GB memory machine. The remaining experiments are carried out on an AMD Ryzen(TM) 5 3600x CPU @3.80 GHz 6-core 16 GB RAM machine using MATLAB R2020b.

4.1. Quality assessment metrics for MEF

Four different perceptual quality metrics, namely, multi-scale structural-similarity (MEF-SSIM) [32], naturalness image quality evaluator (NIQE) [33], blind/referenceless image spatial quality evaluator (BRISQUE) [34,35] and perception based image quality evaluator (PIQE) [36,37], are employed for statistical evaluation. These metrics are chosen since they are commonly used in image enhancement applications and particularly MEF-SSIM is widely preferred in MEF studies.

The MEF-SSIM metric measures the patch structural consistency via the structural-similarity metric (SSIM) [38] and outputs a score in the range [0,1], where results closer to 1 indicate better perceptual quality. Only the contrast and structure components of distinct input exposures are considered while forming a structural comparison element (S) in Eq. (5) and luminance is neglected due to under/over exposedness in patches [3].

$$S(\{x_n\}, y) = (2\sigma_{\hat{x}y} + C)/(\sigma_{\hat{x}}^2 + \sigma_y^2 + C). \tag{5}$$

In Eq. (5), the collocated set of patches in all N images in the input stack are demonstrated with $\{x_n\}$ and the corresponding patch in the output (fused) image is indicated by y. C is a small constant which deals with the low contrast saturation effects [38]. $\hat{x} = \hat{c} \cdot \hat{s}$ represents the desired output patch as a function of the desired contrast $\hat{c}$ and structure $\hat{s}$. $\sigma_{\hat{x}}^2$ and σ_y^2 denote the local variances of $\hat{x}$ and y respectively, while $\sigma_{\hat{x}y}$ represents the local covariance between $\hat{x}$ and y. A spatial quality map is formed using all local patches and the overall MEF-SSIM score is obtained via averaging these local values. The luminance consistency is further taken into account via a set of scale-level scores. It is worth mentioning here that there exists a modified version of MEF-SSIM which is introduced by Fang et al. [31] for dynamic scenes. The fused output is separated into static and dynamic regions, and then the quality measurements of these regions are combined to produce an overall MEF-SSIM score. This version is used in the evaluation of dynamic scenes in this study.

Another metric used is NIQE, which is a space domain natural scene statistic (NSS) driven blind opinion- and distortion-unaware quality assessment method, i.e., it does not need training on databases of human judgments of distorted images and depends only on image models or exposure to naturalistic source images [33]. NIQE is based on the formation of quality aware features and their fit to a multivariate Gaussian model. Similar to NIQE, BRISQUE is also an NSS driven no-reference quality assessment technique [35]. BRISQUE computes point-wise statistics of local normalized luminance and makes use of measured deviations from a natural image model to determine the image naturalness. The last metric employed is the opinion-unaware method PIQE, which does not require training data to measure distortions in images [36]. By taking the advantage of human perception of distortions, local blocks of the input image are classified as distorted or not, and a score is assigned to each block. The mean of these local values provides an overall PIQE score in the range between 0 and 100. For NIQE, BRISQUE and PIQE, the smaller scores indicate better perceptual quality.

4.2. Experimental results and discussion

In order to analyze PCA, adaptive well-exposedness (AWE) and saliency features, the weight maps are employed individually (as well as pairwise) to guide the fusion process. All 38 stacks listed in Tables 1 and 2 are tested and the statistical scores obtained are summarized in Table 3.

It is observed that there exists very slight differences in terms of NIQE, BRISQUE and PIQE scores. On the other side, PAS-MEF outperforms the distinct and pairwise use of weight maps with the MEF-SSIM score, both on average and several times on individual sequences. In particular, alongside presenting the best average MEF-SSIM result, the combination of all three weights produces the minimum MEF-SSIM score. Moreover, as seen from the average MEF-SSIM scores, using the saliency weight, which has a correspondence in the human visual system, increases the performance of weight combinations consistently, whereas using this weight individually results in a much lower MEF-SSIM score than PAS-MEF. Also, the slight increase in execution time due to using three different weights is compensated by the visually appealing output images. Hence, the combination of three map extraction methods is more efficient to guide the fusion process.

For static image fusion, MEF-SSIM scores and the average runtime (in sec) are reported in Table 4 and NIQE, BRISQUE and PIQE scores are provided in Table 5. As it can be clearly observed, PAS-MEF produces very competitive MEF-SSIM scores. On average, PAS-MEF is the second-best performing algorithm. In particular, PAS-MEF presents the best MEF-SSIM scores in five of the static input stacks and its worst score for an individual stack is better than the worst result of most of the algorithms in Table 4. Furthermore, it achieves the third-best BRISQUE score on average while its NIQE and PIQE scores surpass several existing methods (Table 5). As presented in Table 4, several existing MEF algorithms are slightly faster than PAS-MEF, however although it is not optimized yet PAS-MEF outperforms all methods except of Li20, which compensates for the slightly higher execution time.

The statistical scores for dynamic image fusion are reported in Table 6. PAS-MEF presents its effectiveness for also dynamic con-

Table 3
Statistical comparison of the weights used in the fusion process. Average execution time of each step is provided in the last column.

	Min				Max				Avg				
Weight map	MEF-SSIM	NIQE	BRISQUE	PIQE	MEF-SSIM	NIQE	BRISQUE	PIQE	MEF-SSIM	NIQE	BRISQUE	PIQE	Time (s)
PCA	0.869	1.684	4.482	19.024	0.988	4.670	42.372	56.849	0.933	2.667	21.685	38.339	0.076
AWE	0.914	1.200	2.126	16.705	0.996	5.739	43.350	57.076	0.972	2.661	23.100	38.276	0.017
Saliency	0.890	1.748	5.675	18.066	0.993	4.974	43.234	56.303	0.953	2.664	23.040	37.715	0.351
PCA & AWE	0.909	1.607	3.708	16.717	0.995	5.770	43.374	57.365	0.972	2.689	23.243	38.335	0.130
PCA & Saliency	0.893	1.622	2.976	17.821	0.992	4.897	42.766	57.495	0.952	2.666	22.872	38.658	0.453
AWE & Saliency	0.917	1.694	2.521	16.808	0.996	5.761	43.367	57.177	0.973	2.703	23.240	38.219	0.352
PAS-MEF	0.919	1.599	5.142	16.777	0.995	5.836	43.383	57.283	0.974	2.700	23.351	38.408	0.651

Table 4
Static scenes. Statistical comparison of different methods via MEF-SSIM. Best scores are highlighted in bold.

Image Sequence	Mertens09	Li13	Paul16	Nejati17	Ma17	Kou17	Lee18	Hayat19	Li20	Yang20	Ulucan21	PAS-MEF
Arno	**0.991**	0.969	0.958	0.985	0.980	0.971	0.987	0.989	0.990	0.960	0.986	0.989
Chinese Garden	0.989	0.984	0.982	0.991	0.985	0.983	0.990	0.993	**0.994**	0.958	0.991	0.993
Church	0.989	**0.992**	0.978	0.991	**0.992**	**0.992**	**0.992**	**0.992**	**0.992**	0.900	0.989	0.991
Farmhouse	0.981	0.985	0.971	0.983	0.984	0.982	0.979	0.984	**0.986**	0.906	0.979	0.981
Flowers	0.994	0.989	0.961	0.992	0.987	0.992	0.990	**0.995**	**0.995**	0.932	0.990	0.990
IzmirCordon	0.988	0.990	**0.994**	0.986	0.988	0.989	0.988	0.990	0.991	0.942	0.975	0.992
IzmirFair	0.984	0.985	0.983	0.991	0.992	0.985	0.990	0.993	**0.996**	0.983	0.992	0.995
Kluki	0.980	0.968	0.952	0.972	0.970	0.971	0.975	0.980	**0.983**	0.923	0.963	0.979
Landscape	0.976	0.942	0.972	0.992	**0.993**	0.947	0.981	0.973	0.988	0.979	0.986	0.983
Laurenziana	0.988	0.987	0.982	0.987	0.985	0.984	0.987	0.989	0.990	0.963	0.990	**0.991**
Lighthouse	0.980	0.950	0.965	0.975	0.970	0.970	0.979	0.974	0.978	0.926	0.974	**0.982**
Mask	0.987	0.979	0.975	0.988	0.988	0.976	0.990	**0.992**	**0.992**	0.937	0.987	**0.992**
Office	0.984	0.967	0.973	0.988	0.988	0.984	**0.991**	0.987	0.990	0.972	**0.991**	0.984
OldHouse	0.983	0.981	0.973	0.988	0.987	0.990	0.990	0.968	0.990	0.982	0.991	**0.992**
Ostrow	0.974	0.967	0.968	0.979	0.967	0.976	0.978	0.980	0.979	0.950	0.970	**0.982**
Set	0.986	0.960	0.975	0.988	0.988	0.965	0.983	0.990	**0.992**	0.973	0.987	0.990
Tower	0.986	0.986	0.977	0.986	0.986	0.986	0.987	0.987	**0.988**	0.915	0.982	0.983
Treeunil	0.950	0.956	0.864	0.948	0.936	**0.963**	0.956	0.945	0.943	0.713	0.875	0.935
Venice	0.966	0.954	0.954	0.976	0.940	0.952	0.972	0.972	**0.984**	0.948	0.978	0.981
Window	**0.982**	0.971	0.962	0.981	**0.982**	0.972	0.981	**0.982**	**0.982**	0.935	0.979	0.980
YellowHall	0.995	0.990	0.987	0.996	0.995	0.987	0.995	0.994	**0.997**	0.983	0.982	0.995
Avg	0.983	0.974	0.967	0.984	0.980	0.977	0.984	0.983	**0.987**	0.937	0.978	0.985
Time (s)	0.269	0.351	0.442	0.158	3.213	0.599	0.401	0.892	0.312	**0.090**	2.877	0.667

tent, by outperforming most of the methods employed for comparison in terms of MEF-SSIM score by reaching the second-best result on average. Moreover, it presents competitive NIQE, BRISQUE and PIQE scores among others. Additionally, the outcome images of dynamic PAS-MEF are ghosting-free. In the remainder, several visual comparisons are provided for both static and dynamic image sequences, where corresponding MEF-SSIM scores are given in parenthesis in all figures.

In Fig. 4, visual comparisons are presented for the static *Chinese Garden* stack. While the sky area is slightly saturated in Ulucan21, PAS-MEF recovers this region successfully. Moreover, the bush on the bottom right has more well-settled colors in PAS-MEF when compared to Hayat19. PAS-MEF produces better NIQE and BRISQUE results, which indicate superior perceptual quality than Hayat19 and Ulucan21.

The visual comparison for the *IzmirFair* stack is presented in Fig. 5. PAS-MEF and Ma17 recover the cloud behind the statue and the flowers on the foreground successfully, while Yang20 loses several details and produces a noisy output. Moreover, Ma17 produces a dark statue, whereas PAS-MEF recovers this area with more vivid colors. Statistically PAS-MEF produces a superior MEF-SSIM score of 0.995, while Ma17 and Yang20 present scores of 0.992 and 0.983, respectively.

In Fig. 6, the visual outcomes are provided for the *Kluki* stack. As it can be observed from the figure, PAS-MEF produces more vivid colors on the grass regions. Moreover, while the rooftop and the door of the house contain more faded and slightly oversaturated colors in Hayat19 and Paul16, PAS-MEF outputs relatively appealing and well-settled colors in these areas.

Visual comparisons for the *Landscape* stack can be observed in Fig. 7. While colors are faded and details are partially lost throughout the image in Paul16 and under-saturated tree regions can be observed in Ma17, PAS-MEF recovers these details successfully and preserves the naturalness of colors. Statistically, PAS-MEF produces a better PIQE score compared to Paul16 and Ma17.

In Fig. 8, visual results are provided for the *Laurenziana* stack. While the sky region is lightly over-exposed in Ulucan21, Lee18 and PAS-MEF output visually more appealing colors in this region. Moreover, while the tower on the right is slightly under-exposed in Lee18 and over-exposed in Ulucan21, it has a well-settled and vivid color in PAS-MEF. PAS-MEF presents a superior MEF-SSIM score compared to all algorithms (Table 4).

The visual comparison for the *Lighthouse* sequence is given in Fig. 9. PAS-MEF presents the best MEF-SSIM score for this stack as it can be observed in Table 4. While details and color information are severely damaged on the sky and the beach in Paul16, PAS-MEF presents more vivid colors and preserves the details properly. Furthermore, Li20 outputs dark regions on the rooftop of the house and rocks on the beach, whereas PAS-MEF recovers the color information successfully and presents a natural-looking fusion result.

In Fig. 10, visual outputs are provided for the *Mask* stack. While Li20 produces dark regions especially in the building and loses several details, Hayat19 and PAS-MEF recover these areas efficiently. Statistically, all three algorithms reach a high MEF-SSIM score of 0.992; however PAS-MEF outperforms both in terms of NIQE, BRISQUE and PIQE scores.

Visual results of the *OldHouse* sequence are demonstrated in Fig. 11. Mertens09 produces dark regions on the roof area, whereas

Table 5
Static scenes. Statistical comparison of different methods via NIQE, BRISQUE and PIQE. Best scores are highlighted in bold.

	Mertens09			Li13			Paul16			Nejati17		
Image sequence	NIQE	BRISQUE	PIQE	NIQE	BRISQUE	PIQE	NIQE	BRISQUE	PIQE	NIQE	BRISQUE	PIQE
Arno	2.868	27.927	38.266	2.907	**20.575**	37.066	2.944	22.982	**35.082**	2.927	29.207	37.658
Chinese Garden	2.129	17.636	33.680	1.961	9.636	35.591	1.847	19.303	31.900	1.978	25.428	34.516
Church	5.697	43.416	58.814	5.569	43.379	56.359	5.397	43.429	52.460	6.144	43.435	57.727
Farmhouse	2.985	27.782	45.884	3.162	21.657	47.679	2.910	27.074	**41.915**	3.042	25.317	46.128
Flowers	1.728	22.497	18.713	1.578	22.424	18.354	1.893	26.864	**17.062**	1.915	24.914	20.749
IzmirCordon	3.526	32.435	46.634	3.263	**9.991**	21.973	3.166	25.502	38.876	3.231	31.619	44.762
IzmirFair	4.775	24.122	43.609	4.435	26.300	42.018	4.323	**12.776**	40.699	4.777	26.625	42.705
Kluki	2.039	23.332	40.035	1.960	22.961	41.389	**1.714**	24.522	34.631	1.991	23.562	42.334
Landscape	2.702	21.867	**27.867**	2.655	22.457	28.875	2.908	23.468	30.998	2.680	18.277	30.192
Laurenziana	2.534	22.312	41.262	2.496	21.131	**39.689**	2.582	**10.289**	40.760	2.468	22.401	41.785
Lighthouse	2.794	**15.036**	37.161	2.715	16.816	36.588	**2.701**	24.295	**34.336**	2.911	17.495	41.681
Mask	3.081	24.182	34.236	2.761	23.426	33.940	2.827	**3.411**	33.096	3.055	20.758	35.848
Office	3.055	**24.206**	52.710	3.100	29.245	51.521	2.975	42.849	51.196	2.891	32.795	53.049
OldHouse	1.834	20.471	32.404	1.780	**7.100**	31.064	1.703	25.081	**30.453**	1.583	13.718	31.571
Ostrow	3.024	21.180	53.156	2.526	**16.449**	44.387	**2.282**	26.532	**36.234**	2.422	17.695	46.664
Set	3.756	32.615	41.104	3.394	28.360	42.313	3.355	26.884	**40.619**	3.253	25.572	43.181
Tower	2.204	21.843	31.284	2.239	20.832	27.447	2.097	22.517	**25.753**	2.327	27.767	30.611
Treeunil	**1.608**	**12.107**	**23.346**	2.296	23.566	34.102	1.892	18.391	25.741	2.437	16.654	32.857
Venice	3.476	27.011	50.545	3.125	15.790	46.338	2.536	23.132	47.561	3.311	25.263	49.390
Window	2.326	24.123	35.836	2.294	25.310	37.835	2.465	**6.492**	**34.591**	**2.284**	24.079	34.827
YellowHall	3.127	12.367	45.143	3.114	**11.774**	44.000	3.191	20.398	**33.549**	3.126	11.841	48.313
Avg	2.918	23.737	39.604	2.825	**20.913**	38.025	2.748	22.676	**36.072**	2.893	24.020	40.312
	Ma17			Kou17			Lee18			Hayat19		
Image sequence	NIQE	BRISQUE	PIQE	NIQE	BRISQUE	PIQE	NIQE	BRISQUE	PIQE	NIQE	BRISQUE	PIQE
Arno	3.056	25.337	39.802	2.922	26.158	40.319	**0.301**	22.740	37.120	3.025	24.118	37.571
Chinese Garden	1.923	16.825	34.571	2.069	8.207	33.515	2.056	**8.179**	34.085	1.947	16.406	34.626
Church	5.668	43.410	57.236	5.212	43.148	56.299	5.489	43.330	57.339	5.822	43.420	57.294
Farmhouse	3.125	21.962	48.022	3.006	27.951	48.118	2.969	28.788	47.420	3.067	28.506	48.919
Flowers	1.720	24.768	19.644	1.781	21.515	19.129	**1.509**	21.817	18.281	1.661	22.387	19.476
IzmirCordon	3.336	31.439	46.308	3.172	10.691	**20.911**	3.227	31.576	46.422	3.369	31.889	46.282
IzmirFair	4.264	24.567	42.022	4.198	23.716	41.932	4.150	24.481	41.324	4.590	25.137	40.945
Kluki	2.064	23.530	42.529	2.023	23.105	42.428	2.025	22.646	41.226	1.984	22.758	42.272
Landscape	2.548	20.820	30.283	2.661	21.784	29.807	2.655	22.236	28.964	2.658	22.546	28.492
Laurenziana	2.481	22.221	39.974	2.417	19.626	40.995	2.550	20.799	40.260	2.507	21.901	40.670
Lighthouse	2.889	19.310	41.866	2.790	18.991	36.141	2.752	19.176	37.213	2.702	16.378	36.837
Mask	2.874	23.594	35.028	2.883	23.359	34.904	2.885	23.353	31.781	2.889	22.990	33.680
Office	3.147	40.429	53.707	3.005	33.757	52.915	2.822	37.080	53.787	2.971	34.336	53.056
OldHouse	1.618	14.505	33.181	1.670	7.296	33.536	1.706	9.342	33.521	1.768	15.551	35.950
Ostrow	2.527	20.191	48.786	2.443	20.684	48.119	2.384	22.721	47.410	2.816	23.943	50.846
Set	3.354	25.436	47.063	3.359	24.501	45.199	3.457	26.597	49.229	3.286	25.136	45.095
Tower	2.296	26.876	31.281	2.245	21.933	29.704	2.306	19.285	30.313	2.317	19.439	30.458
Treeunil	2.373	35.766	31.420	2.357	30.725	32.203	2.314	28.869	31.729	2.578	35.539	36.042
Venice	3.292	24.662	49.114	3.197	15.991	47.074	3.318	6.759	43.777	3.251	22.628	48.036
Window	2.447	25.487	36.352	2.366	24.664	37.436	2.414	23.072	38.332	2.431	22.832	37.495
YellowHall	3.094	13.026	48.536	3.158	14.869	49.493	3.099	14.332	47.108	3.094	11.804	46.254
Avg	2.862	24.960	40.796	2.806	22.032	39.056	2.804	22.723	39.840	2.892	24.269	40.490
	Li20			Yang20			Ulucan21			PAS-MEF		
Image Sequence	NIQE	BRISQUE	PIQE	NIQE	BRISQUE	PIQE	NIQE	BRISQUE	PIQE	NIQE	BRISQUE	PIQE
Arno	3.006	23.550	41.231	2.794	29.072	38.930	3.040	27.905	39.987	2.965	21.965	37.427
Chinese Garden	2.137	18.776	32.512	**1.739**	18.640	**31.182**	1.942	9.109	35.977	1.937	6.919	34.446
Church	5.721	43.313	57.220	**4.679**	**36.796**	**49.185**	5.486	43.260	56.179	5.836	43.383	57.283
Farmhouse	3.151	**18.298**	48.316	**2.689**	29.544	44.599	2.965	30.075	48.973	2.952	29.349	48.716
Flowers	1.779	24.620	20.066	2.583	23.386	23.088	1.836	23.133	19.099	1.599	**19.855**	18.043
IzmirCordon	3.350	32.513	48.068	**2.874**	34.586	40.196	3.197	31.361	46.779	3.364	32.111	48.066
IzmirFair	4.779	25.393	41.021	**3.139**	26.685	**40.218**	4.240	24.808	40.807	4.012	23.509	42.464
Kluki	2.100	23.270	39.746	2.166	23.886	**31.183**	2.077	**22.527**	43.047	2.138	22.615	41.792
Landscape	2.726	**17.618**	30.428	2.559	25.563	30.061	**2.487**	19.511	32.631	2.612	22.450	29.005
Laurenziana	2.538	22.237	41.236	**2.239**	21.724	38.390	2.381	22.741	40.160	2.473	20.346	39.648
Lighthouse	2.854	17.346	37.901	2.436	30.145	36.639	2.804	20.911	39.933	2.772	18.659	39.089
Mask	3.288	22.338	36.501	**1.932**	26.715	**28.553**	2.775	23.303	37.002	2.748	21.014	32.967
Office	2.895	26.359	53.077	3.050	33.216	**49.564**	2.906	26.008	54.324	**2.758**	40.183	54.391
OldHouse	1.713	10.769	32.253	1.936	23.935	32.838	**1.578**	14.444	34.477	1.709	14.557	33.955
Ostrow	3.192	23.229	54.270	3.144	24.847	39.974	2.573	21.934	45.014	2.623	25.063	48.569
Set	3.440	25.424	45.013	**3.179**	27.654	51.794	3.342	**24.234**	48.250	3.283	24.266	45.898
Tower	2.233	21.483	31.764	**2.096**	14.671	28.013	2.345	22.468	30.422	2.331	**11.991**	29.732
Treeunil	3.126	29.707	41.589	1.966	28.340	29.895	1.889	31.588	25.516	2.438	31.936	24.986
Venice	3.297	27.101	46.377	**2.919**	10.794	**36.561**	3.437	12.710	44.999	3.368	**5.142**	45.201
Window	2.488	23.143	37.010	3.288	22.085	42.182	2.572	24.539	38.139	2.600	21.185	39.253
YellowHall	3.178	12.059	45.857	**2.873**	15.023	51.608	3.120	11.995	47.726	3.136	13.812	49.857
Avg	3.000	23.264	41.022	**2.680**	37.569	37.841	2.809	23.265	40.450	2.841	22.396	39.547

Table 6
Dynamic scenes. Statistical comparison of different methods via MEF-SSIM, NIQE, BRISQUE and PIQE. Best scores are highlighted in bold.

	Hu13				Li14				Qin14				Ma17			
Image sequence	MEF-SSIM	NIQE	BRISQUE	PIQE	MEF-SSIM	NIQE	BRISQUE	PIQE	MEF-SSIM	NIQE	BRISQUE	PIQE	MEF-SSIM	NIQE	BRISQUE	PIQE
Arch	0.948	1.934	19.668	24.139	0.935	**1.580**	5.882	21.612	0.859	1.685	**4.819**	**19.188**	**0.983**	1.966	8.685	20.241
Brunswick	0.966	2.221	16.077	42.611	0.959	2.195	16.072	42.125	0.902	1.992	18.647	**40.176**	**0.975**	2.365	19.208	43.843
Campus	0.954	2.059	9.897	29.053	0.952	2.275	16.306	26.208	0.922	**1.764**	23.119	27.055	0.961	1.924	22.620	27.086
Cliff	0.870	2.902	30.680	30.157	0.981	2.982	21.582	29.448	0.817	**2.412**	30.251	**25.504**	**0.986**	2.997	20.484	33.077
Forest	0.886	**3.231**	**23.886**	34.528	0.921	4.117	32.744	40.819	0.809	3.576	19.684	**31.708**	**0.962**	3.715	32.793	43.301
Horse	0.945	2.882	32.005	34.134	0.938	2.734	28.783	**31.992**	0.894	2.903	**22.315**	35.065	**0.971**	2.765	29.826	35.407
Lady	0.916	2.332	15.344	42.847	0.923	2.621	**11.045**	41.032	0.856	2.491	38.107	58.534	0.928	2.820	30.969	**26.343**
Llandudno	0.958	2.527	36.777	50.988	0.988	2.694	32.846	47.273	0.916	**2.499**	36.748	50.004	0.986	3.016	33.485	50.840
ProfJeonEight	0.922	2.302	22.522	41.981	0.923	2.221	17.983	43.057	0.885	2.097	31.707	41.868	0.947	2.346	28.312	34.225
Pupptes	0.933	2.306	9.683	25.604	0.934	2.190	19.786	25.827	0.850	**1.641**	25.037	32.977	**0.958**	2.414	22.908	26.893
ReadingMan	0.967	2.538	28.137	22.787	0.962	2.401	35.253	29.669	0.927	2.840	32.326	53.049	0.971	**2.145**	29.175	20.824
Russ1	0.970	2.785	16.366	23.833	0.966	2.862	16.855	22.207	0.917	**2.608**	**14.564**	26.386	**0.979**	2.895	21.984	**20.643**
SculptureGarden	0.917	**1.957**	18.035	35.834	0.915	2.230	8.316	**33.961**	0.762	2.307	27.915	34.348	0.948	2.214	8.090	36.424
Square	0.973	1.929	27.335	39.532	0.965	1.978	25.385	39.270	0.918	**1.790**	28.825	**36.544**	**0.987**	2.151	28.462	40.673
Tate3	0.953	2.263	24.221	43.259	0.951	2.119	28.979	42.921	0.909	**2.049**	29.591	41.383	0.942	2.247	28.620	42.655
Wroclav	0.896	2.372	28.517	41.480	0.954	**2.063**	21.841	42.747	0.856	2.163	30.402	**39.300**	**0.972**	2.149	30.082	43.868
YWFusionopolis	0.876	1.902	20.268	36.429	0.877	**1.779**	**16.102**	37.769	0.839	1.807	17.965	32.886	0.891	2.246	11.771	38.840
Avg	0.932	2.379	22.319	35.247	0.944	2.414	**20.927**	35.173	0.873	**2.272**	25.413	36.822	**0.962**	2.493	23.969	**34.423**
	Hayat19				Li20				Qi20				PAS-MEF			
Image sequence	MEF-SSIM	NIQE	BRISQUE	PIQE	MEF-SSIM	NIQE	BRISQUE	PIQE	MEF-SSIM	NIQE	BRISQUE	PIQE	MEF-SSIM	NIQE	BRISQUE	PIQE
Arch	0.953	2.096	14.317	19.985	0.976	2.056	20.335	21.082	0.975	1.947	5.001	19.621	0.937	1.812	14.718	24.165
Brunswick	0.859	2.315	19.495	46.383	0.969	2.138	**15.662**	45.757	0.838	2.502	17.058	44.657	0.972	**1.934**	24.759	40.313
Campus	0.881	2.175	**7.519**	25.136	0.923	2.036	19.578	26.419	0.958	2.292	9.067	**23.684**	**0.963**	2.058	24.142	36.026
Cliff	0.887	2.737	**19.109**	32.735	0.981	3.049	23.106	32.830	0.975	2.824	21.664	32.381	0.981	3.013	21.108	32.878
Forest	0.896	3.797	31.401	41.395	0.950	3.748	32.624	42.629	0.958	4.208	36.851	45.825	0.950	3.983	33.783	44.851
Horse	0.758	2.757	29.496	39.888	0.969	2.723	27.546	35.035	0.960	**2.694**	23.993	36.342	0.932	3.075	30.186	35.051
Lady	0.822	2.626	35.581	26.711	0.827	**2.172**	25.306	51.985	0.782	2.513	19.012	49.769	**0.974**	2.995	24.142	36.026
Llandudno	0.907	2.614	32.111	48.810	0.993	2.982	33.742	50.049	0.879	3.063	32.876	49.808	**0.994**	2.518	**30.594**	**46.015**
ProfJeonEight	0.848	2.121	21.070	**32.365**	0.885	2.218	**16.242**	47.124	**0.952**	**2.010**	20.745	42.728	0.932	2.463	33.124	38.092
Pupptes	0.835	2.399	**6.788**	27.808	0.951	2.240	8.405	32.474	0.933	2.416	18.799	**25.053**	0.921	2.528	22.334	25.067
ReadingMan	0.828	2.266	30.521	19.062	0.966	2.366	33.286	30.914	0.964	2.621	27.987	26.376	**0.974**	2.208	**27.615**	**16.777**
Russ1	0.871	2.844	15.932	25.795	0.978	2.782	21.429	21.167	0.856	3.127	24.064	23.026	0.975	2.748	15.256	25.283
SculptureGarden	0.835	2.177	10.059	36.678	**0.954**	2.359	**6.423**	39.308	0.922	2.197	12.982	34.810	0.919	2.165	25.622	39.653
Square	0.902	2.153	29.241	41.744	0.986	2.028	21.055	40.950	0.857	2.250	**14.379**	41.779	0.980	1.834	30.867	38.160
Tate3	0.831	2.174	24.602	45.405	0.859	2.254	17.666	45.485	0.893	2.324	19.112	**39.827**	**0.969**	2.054	**14.811**	40.179
Wroclav	0.813	2.465	**14.438**	46.359	0.968	2.189	22.499	46.306	0.824	2.217	29.625	45.802	0.936	2.320	23.821	47.269
YWFusionopolis	0.813	2.179	21.719	**30.470**	0.867	1.841	18.429	38.320	0.827	1.879	22.852	38.299	**0.962**	1.992	20.755	36.584
Avg	0.855	2.464	21.376	34.513	0.941	2.422	21.373	38.108	0.903	2.534	20.945	36.458	0.957	2.453	24.567	35.435

(a) Three input exposures in the stack.

(b) Hayat19 (0.993) (c) Ulucan21 (0.991) (d) PAS-MEF (0.993)

Fig. 4. Visual comparison of PAS-MEF with Hayat19 and Ulucan21 for *Chinese Garden*.

(a) Three input exposures in the stack.

(b) Yang20 (0.983) (c) Ma17 (0.992) (d) PAS-MEF (0.995)

Fig. 5. Visual comparison of PAS-MEF with Yang20 and Ma17 for *IzmirFair*.

Lee18 and PAS-MEF recover these areas successfully. Overall, PAS-MEF outputs a more natural-looking fusion image with well-settled colors. In terms of MEF-SSIM, PAS-MEF suppresses all algorithms with a high score of 0.992.

In Fig. 12, visual comparisons are illustrated for the *Set* sequence. Ulucan21 produces bright areas in the sky region and around the lights, while PAS-MEF presents more natural-looking colors in these regions. Compared to Paul16, PAS-MEF outputs an image with more vivid and well-settled colors, which may also affect the MEF-SSIM scores. Paul16 reaches a MEF-SSIM score of 0.975 and PAS-MEF achieves a high score of 0.990.

The visual comparison is demonstrated for the *Tower* stack in Fig. 13. While the tower contains under-saturated regions and consequently suffers from detail loss both in Mertens09 and Li20, PAS-MEF recovers the tower successfully and produces a visually more appealing result. Additionally, the colors of the flowers on the fore-

(a) Three input exposures in the stack.

(b) Hayat19 (0.980) (c) Paul16 (0.952) (d) PAS-MEF (0.979)

Fig. 6. Visual comparison of PAS-MEF with Hayat19 and Paul16 for *Kluki*.

(a) Three input exposures in the stack.

(b) Paul16 (0.972) (c) Ma17 (0.993) (d) PAS-MEF (0.983)

Fig. 7. Visual comparison of PAS-MEF with Paul16 and Ma17 for *Landscape*.

ground appear to be faded In Mertens09, but PAS-MEF presents more vivid colors in this region. On the other side, Mertens09 and Li20 both preserve the details on the bright clouds on the left successfully, however PAS-MEF outputs a slightly over-exposed clouds.

The visual results for the *Treeunil* stack are presented in Fig. 14. This sequence has 7 input images containing severely over- and under-exposed regions, which makes it hard to preserve details for most of the methods discussed in Section 2. While the sky region contains severely over-exposed regions, the tree has strong shadows which affect the visual and statistical results of all algorithms. The best MEF-SSIM score is 0.963 and it is obtained by Kou17. The output of Li13 contains halo effects, and the fused images of Li20 and PAS-MEF face a challenge in over-exposed regions. Besides, PAS-MEF presents higher outcomes than these methods in terms of the PIQE score.

The comparison for *Venice* is presented in Fig. 15. PAS-MEF recovers the sky region efficiently by producing a more natural-looking output, while Ulucan21 presents a brighter sky and several details are lost due to excessive luminosity. Furthermore, Li20 demonstrates a slightly higher MEF-SSIM score than PAS-MEF. However, in contrary to Li20, PAS-MEF avoids to output low-light regions, thus presents the fine details in the image better than Li20.

In Fig. 16, visual outcomes are given for the *YellowHall* sequence. Nejati17 presents an output in which the left part of the image is relatively darker compared to its right side, while both Mertens09 and PAS-MEF produce a fusion with more balanced and well-settled colors. In Mertens09, the ceiling has a more brighter color than PAS-MEF. Statistically, all three algorithms demonstrate very similar MEF-SSIM results, but PAS-MEF outperforms them in terms of NIQE score.

The exposure stack and visual outputs are demonstrated for the dynamic *Cliff* sequence in Fig. 17. While the texture of the rock on the cliff and the rocks at the seaside are faded both in Li14 and Hayat19, PAS-MEF preserves these fine details successfully. Although statistical results are competitive for all algorithms, Hayat19 produces a more over-exposed result and Li14 produces color distortions at the small cave. PAS-MEF creates a more vivid-looking image while covering the details on the mentioned regions without sacrificing the color correlation.

(a) Three input exposures in the stack.

(b) Lee18 (0.987) (c) Ulucan21 (0.990) (d) PAS-MEF (0.991)

Fig. 8. Visual comparison of PAS-MEF with Lee18 and Ulucan21 for *Laurenziana*.

(a) Three input exposures in the stack.

(b) Paul16 (0.965) (c) Li20 (0.978) (d) PAS-MEF (0.982)

Fig. 9. Visual comparison of PAS-MEF with Paul16 and Li20 for *Lighthouse*.

(a) Three input exposures in the stack.

(b) Hayat19 (0.992) (c) Li20 (0.992) (d) PAS-MEF (0.992)

Fig. 10. Visual comparison of PAS-MEF with Hayat19 and Li20 for *Mask*.

(a) Three input exposures in the stack.

(b) Mertens09 (0.983) (c) Lee18 (0.990) (d) PAS-MEF (0.992)

Fig. 11. Visual comparison of PAS-MEF with Mertens09 and Lee18 for *OldHouse*.

Visual results of the dynamic *Llandudno* sequence are shown in Fig. 18. Ma17 produces ghosting artifacts in the region where people are preparing the tables, whereas Li20 and PAS-MEF produce ghosting-free outputs. PAS-MEF preserves the details successfully and creates a more natural-looking image with a surpassing high MEF-SSIM score of 0.994.

The visual comparison for the dynamic *ReadingMan* stack is presented in Fig. 19. While Ma17 produces an outcome with several artifacts on the T-shirt and glasses of the man, PAS-MEF recovers these areas successfully. Furthermore, PAS-MEF preserves the push sign on the door, whereas Hu13 fails to preserve this detail. On the other hand, Hu13 recovers the color information in small parts of the white T-shirt and the wall better than PAS-MEF. Overall, PAS-MEF outperforms all algorithms in terms of MEF-SSIM, BRISQUE and PIQE.

In Fig. 20, visual results are provided for the dynamic *Square* stack. While Hayat19 and Qin14 produce images with ghosting artifacts, PAS-MEF creates a ghosting-free image. The artifacts are also significantly visible in the sky region for Qin14, whereas Hayat19 and PAS-MEF create a more natural-looking sky. In addition, PAS-MEF recovers texture details of the buildings which results in a higher statistical score compared to Hayat19 and Qin14.

Visual outputs for the dynamic *YWFusionopolis* sequence are demonstrated in Fig. 21. It can be observed that the color of the grass is faded in Qin14, and it is successfully preserved in Li14 and PAS-MEF. The gray cubic part of the building on the background has lost its natural color in both Li14 and Qin14, whereas this color information is efficiently recovered in PAS-MEF. Furthermore, several artifacts can be seen on the pants of the woman in Li14 and Qin14, while PAS-MEF produces an artifact-free and visually more appealing outcome in this region. PAS-MEF produces the highest MEF-SSIM score and outperforms all other algorithms significantly.

The visual outcomes for the *Campus* stack are demonstrated in Fig. 22. This stack contains severely under- and over-exposed regions, which challenge PAS-MEF in some regions of the scene. Overall, PAS-MEF preserves the details well and produces the highest MEF-SSIM score among the algorithms in Table 6.

A visual comparison for the *Lady* stack is given in Fig. 23. PAS-MEF produces the highest MEF-SSIM score among other algorithms for this sequence. Although more complex methods based on his-

(a) Three input exposures in the stack.

(b) Paul16 (0.975) (c) Ulucan21 (0.987) (d) PAS-MEF (0.990)

Fig. 12. Visual comparison of PAS-MEF with Paul16 and Ulucan21 for *Set*.

(a) Three input exposures in the stack.

(b) Mertens09 (0.986) (c) Li20 (0.988) (d) PAS-MEF (0.983)

Fig. 13. Visual comparison of PAS-MEF with Mertens09 and Li20 for *Tower*.

(a) Seven input exposures in the stack.

(b) Li13 (0.956) (c) Kou17 (0.963) (d) Li20 (0.943) (e) PAS-MEF (0.935)

Fig. 14. Visual comparison of PAS-MEF with Li13, Kuo17 and Li20 for *Treeunil*.

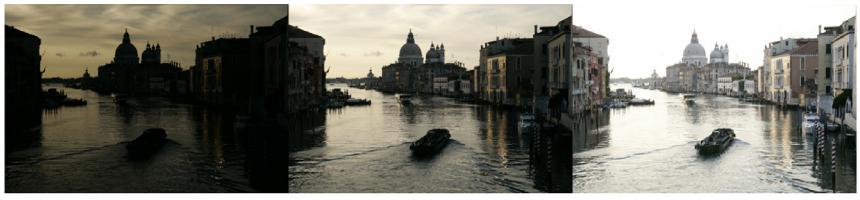

(a) Three input exposures in the stack.

(b) Li20 (0.984) (c) Ulucan21 (0.978) (d) PAS-MEF (0.981)

Fig. 15. Visual comparison of PAS-MEF with Li20 and Ulucan21 for *Venice*.

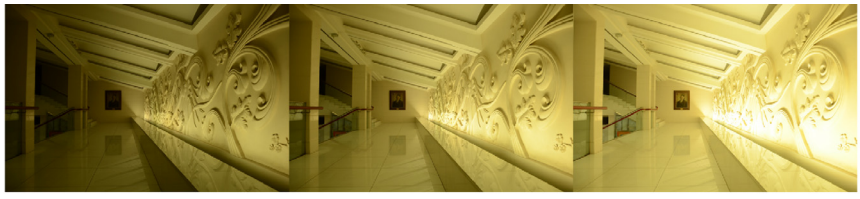

(a) Three input exposures in the stack.

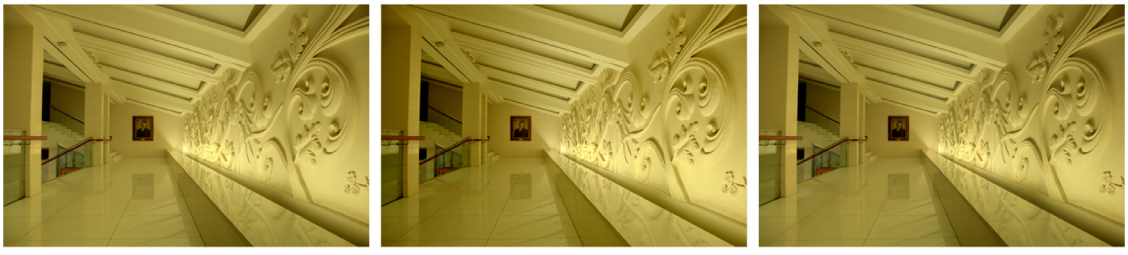

(b) Mertens09 (0.995) (c) Nejati17 (0.996) (d) PAS-MEF (0.995)

Fig. 16. Visual comparison of PAS-MEF with Mertens09 and Nejati17 for *YellowHall*.

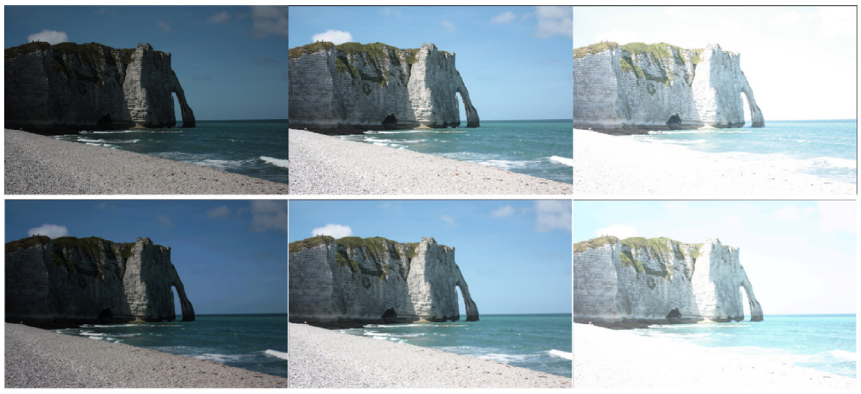

(a) (Top-to-bottom) Three input exposures in the stack and their aligned versions.

(b) Li14 (0.981) (c) Hayat19 (0.887) (d) PAS-MEF (0.981)

Fig. 17. Visual comparison of PAS-MEF with Li14 and Hayat19 for *Cliff*.

(a) (Top-to-bottom) Three input exposures in the stack and their aligned versions.

(b) Ma17 (0.986) (c) Li20 (0.993) (d) PAS-MEF (0.994)

Fig. 18. Visual comparison of PAS-MEF with Ma17 and Li20 for *Llandudno*.

(a) (Top-to-bottom) Three input exposures in the stack and their aligned versions.

(b) Hu13 (0.967) (c) Ma17 (0.971) (d) PAS-MEF (0.974)

Fig. 19. Visual comparison of PAS-MEF with Hu13 and Ma17 for *ReadingMan*.

(a) (Top-to-bottom) Three input exposures in the stack and their aligned versions.

(b) Qin14 (0.918) (c) Hayat19 (0.902) (d) PAS-MEF (0.980)

Fig. 20. Visual comparison of PAS-MEF with Qin14 and Hayat19 for *Square*.

(a) (Top-to-bottom) Six input exposures in the stack and their aligned versions.

(b) Li14 (0.877) (c) Qin14 (0.839) (d) PAS-MEF (0.962)

Fig. 21. Visual comparison of PAS-MEF with Li14 and Qin14 for *YWFusionopolis*.

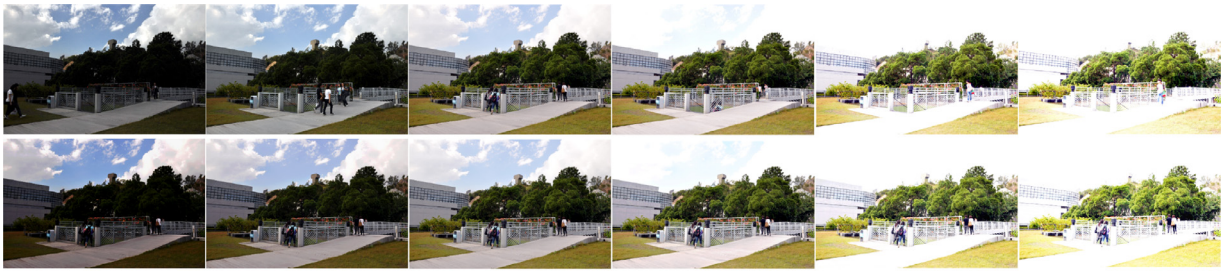

(a) (Top-to-bottom) Six input exposures in the stack and their aligned versions.

(b) Hu13 (0.954) (c) Li14 (0.952) (d) PAS-MEF (0.963)

Fig. 22. Visual comparison of PAS-MEF with Hu13 and Li14 for *Campus*.

tograms such as [39] can be used instead of Eq. (1), it can be clearly observed that the proposed solution is a simple yet effective method to prevent any artifacts and noise when motion is present in the input stack. In the outcomes of both Qin14 and Li20, ambiguities due to non-effective handling of the motion are visible particularly around the head of the person.

4.3. Application to visible and infrared image fusion

Based on the thermal radiance difference, the background and targets can be distinguished in infrared images, which usually have low resolution, but are not affected by poor lightning and bad weather conditions [40]. On the other hand, based on the reflected light, texture information and fine details are provided in accordance with the HVS in visible images, which tend to have high resolution, but are easily disturbed by poor illumination [40]. Considering infrared and visible images have complementary characteristics, the output from their proper fusion will naturally demonstrate an image containing more information than these images individually. Thus, several applications such as object detection, tracking and recognition, remote sensing, surveillance and color vision take advantage of infrared and visible image fusion [40].

In recent years, numerous studies have been conducted related to infrared and visible image fusion. In the work of Liu et al. [41], a method based on convolutional neural networks (CNNs) is proposed to carry out infrared and visible image fusion. A siamese CNNs architecture is modeled to extract a weight map containing the integrated pixel activity information and then fusion is per-

(a) (Top-to-bottom) Three input exposures in the stack and their aligned versions.

(b) Qin14 (0.856) (c) Li20 (0.827) (d) PAS-MEF (0.974)

Fig. 23. Visual comparison of PAS-MEF with Qin14 and Li20 for *Lady*.

formed via a pyramidal approach. Neural networks are also used in the study of Li et al. [42], which takes advantage of ResNet to extract features from input images. These weight maps are normalized through zero-phase component analysis and ℓ_1-norm, and latter processed via a softmax operation. Lastly, fusion is conducted through weighted-averaging. In the study of Bavirisetti et al. [43], a blending method based on guided filter and pixel level fusion is proposed to perform diverse fusion operations. The structure transferring and multi-scale image decomposition property of guided filters is exploited to design a new visual saliency and weight map extraction technique.

In this paper, the application of PAS-MEF is tested in the field of infrared and visible image fusion. It is utilized to fuse infrared and visible images with its default settings and no optimization is carried out on the algorithm. The outputs of PAS-MEF is compared with the studies Liu18 [41], Li19 [42] and Bavirisetti19 [43] through the benchmark of Zhang et al. [44]. Six different image pairs are employed to carry out the experiments. In order to provide statistical analysis two perceptual metrics, namely SSIM [38] and visual information fidelity (VIF) [45] are reported in this study. VIF is based on image distortions, a statistical model for natural scenes and the HVS [45]. It presents scores in the range $[0,\ 1]$, where results closer to 1 indicate better perceptual quality. Table 7 presents the statistical outcomes of infrared and visible image fusion, in which PAS-MEF demonstrates highly competitive results by achieving the second best SSIM and VIF scores on average.

Fig. 24 compares visual outputs and corresponding SSIM scores for the *ElecBike* input pair. While Li19 and PAS-MEF recover the details of the man efficiently, several details are lost in Li18. Furthermore, fine details of trees and bushes both in the foreground and background are successfully preserved by PAS-MEF, whereas information loss is observed in Li19.

Table 7
Infrared and visible image fusion. Statistical comparison of different methods via SSIM and VIF. Best scores are highlighted in bold.

	Liu18		Li19		Bavirisetti19		PAS-MEF	
	SSIM	VIF	SSIM	VIF	SSIM	VIF	SSIM	VIF
CarLight	0.783	0.597	**0.810**	0.437	0.582	**0.639**	0.796	0.539
ElecBike	0.780	0.568	**0.817**	0.427	0.790	**0.581**	0.785	0.575
Man	0.727	**0.531**	**0.768**	0.367	0.737	0.467	0.742	0.527
ManCall	0.759	0.443	**0.813**	0.332	0.773	0.429	0.785	**0.468**
NightCar	0.724	0.475	**0.768**	0.337	0.733	0.432	0.744	**0.487**
Tricycle	0.767	**0.541**	**0.798**	0.376	0.781	**0.541**	0.773	0.518
Avg	0.756	**0.526**	**0.795**	0.379	0.733	0.515	0.771	0.519

(a) Input image pair.

(b) Liu18 (0.780) (c) Li19 (0.817) (d) PAS-MEF (0.785)

Fig. 24. Visual comparison of PAS-MEF with Liu18 and Li19 for *ElecBike*.

(a) Input image pair.

(b) Li19 (0.768) (c) Bavirisetti19 (0.737) (d) PAS-MEF (0.742)

Fig. 25. Visual comparison of PAS-MEF with Li19 and Bavirisetti19 for *Man*.

Visual outputs and SSIM scores of the *Man* input pair are presented in Fig. 25. Overall, Bavirisetti19 and PAS-MEF recover fine details successfully. Even though its higher SSIM score, visual information is lost in Li19, which may also explain its significantly lower VIF score in Table 7.

5. Conclusion

The production of HDR-like content through MEF is a challenging yet useful technology. Since high quality images can be obtained with low computational cost, it is commonly preferred by user-grade device manufacturers. Hence, it is an attractive field of study and numerous methods have been developed in recent years. Although the fusion process of these diverse MEF algorithms are similar, the weight map characterization procedure is different. In order to keep the "best" parts of each exposure, these weight maps are used to eliminate the unsatisfactory regions of each input in the stack. This process becomes more troublesome in case of the presence of local and/or global motion in between the exposure bracket.

To contribute to the development of a general weight map framework, this study introduces a novel weight map characterization scheme based on PCA, adaptive well-exposedness and saliency maps. These weight maps are refined through a guided filter to eliminate possible noise and artifacts. Then, the fusion process is carried out via a pyramidal decomposition. It is important to note here that, to the best of available knowledge, PCA and fully-adaptive well exposedness are introduced to the field of MEF for the first time.

The developed PAS-MEF algorithm is compared extensively with several state-of-the-art methods and it demonstrates very strong visual and statistical results in both static and dynamic cases. In order to observe its effectiveness in different image fusion applications, PAS-MEF is also tested in infrared and visible image fusion. Without any optimization, PAS-MEF presents highly competitive results in this field. As a result, it can be deduced that PAS-MEF may enlighten the path to the design of a general weight map characterization scheme. As a future direction, it is considered to optimize the algorithm to both increase its effectiveness and decrease its computational complexity, and extend its applications to different image fusion problems, such as medical image fusion and multi-focus image fusion.

Declaration of Competing Interest

The authors declare that they have no known competing financial interests or personal relationships that could have appeared to influence the work reported in this paper.

CRediT authorship contribution statement

Oguzhan Ulucan: Conceptualization, Methodology, Software, Validation, Formal analysis, Investigation, Writing – original draft, Visualization. **Diclehan Ulucan:** Conceptualization, Methodology, Software, Validation, Formal analysis, Investigation, Writing – original draft, Visualization. **Mehmet Turkan:** Conceptualization, Methodology, Formal analysis, Writing – review & editing, Supervision.

Acknowledgment

The authors are thankful to Prof. Zhiguang Yang for providing the visual outputs of Yang20.

References

[1] A.O. Akyuz, E. Reinhard, Color appearance in high-dynamic-range imaging, J. Electron. Imaging 15 (3) (2006) 033001.
[2] C. Kiser, E. Reinhard, M. Tocci, N. Tocci, Real time automated tone mapping system for HDRvideo, in: IEEE Int. Conf. Image Process., vol. 134, 2012.
[3] O. Ulucan, D. Karakaya, M. Turkan, Multi-exposure image fusion based on linear embeddings and watershed masking, Signal Process. 178 (2021) 107791.
[4] M. Zheng, G. Qi, Z. Zhu, Y. Li, H. Wei, Y. Liu, Image dehazing by an artificial image fusion method based on adaptive structure decomposition, IEEE Sens. J. 20 (14) (2020) 8062–8072.
[5] Z. Zhu, H. Wei, G. Hu, Y. Li, G. Qi, N. Mazur, A novel fast single image dehazing algorithm based on artificial multiexposure image fusion, IEEE Trans. Instrum. Meas. 70 (-) (2020) 1–23.
[6] T. Mertens, J. Kautz, F. Van Reeth, Exposure fusion: a simple and practical alternative to high dynamic range photography, Comput. Graph. Forum 28 (1) (2009) 161–171.
[7] J. Hu, O. Gallo, K. Pulli, X. Sun, HDR deghosting: how to deal with saturation? in: IEEE Conf. Comput. Vision Pattern Recognit., 2013, pp. 1163–1170.
[8] S. Li, X. Kang, J. Hu, Image fusion with guided filtering, IEEE Trans. Image Process. 22 (2013) 2864–2875.
[9] Z. Li, J. Zheng, Z. Zhu, S. Wu, Selectively detail-enhanced fusion of differently exposed images with moving objects, IEEE Trans. Image Process. 23 (10) (2014) 4372–4382.
[10] X. Qin, J. Shen, X. Mao, X. Li, Y. Jia, Robust match fusion using optimization, IEEE Trans. Cybern. 45 (8) (2014) 1549–1560.
[11] S. Paul, I.S. Sevcenco, P. Agathoklis, Multi-exposure and multi-focus image fusion in gradient domain, J. Circuits Syst. Comput. 25 (10) (2016) 1650123.
[12] M. Nejati, M. Karimi, S.R. Soroushmehr, N. Karimi, S. Samavi, K. Najarian, Fast exposure fusion using exposedness function, in: IEEE Int. Conf. Image Process., 2017, pp. 2234–2238.
[13] F. Kou, Z. Li, C. Wen, W. Chen, Multi-scale exposure fusion via gradient domain guided image filtering, in: IEEE Int. Conf. Multimedia Expo, 2017, pp. 1105–1110.
[14] K. Ma, H. Li, H. Yong, Z. Wang, D. Meng, L. Zhang, Robust multi-exposure image fusion: a structural patch decomposition approach, IEEE Trans. Image Process. 26 (5) (2017) 2519–2532.
[15] H. Li, K. Ma, H. Yong, L. Zhang, Fast multi-scale structural patch decomposition for multi-exposure image fusion, IEEE Trans. Image Process. 29 (2020) 5805–5816.
[16] S.-h. Lee, J.S. Park, N.I. Cho, A multi-exposure image fusion based on the adaptive weights reflecting the relative pixel intensity and global gradient, in: IEEE Int. Conf. Image Process., 2018, pp. 1737–1741.
[17] N. Hayat, M. Imran, Ghost-free multi exposure image fusion technique using dense SIFT descriptor and guided filter, J. Vis. Commun. Image Represent. 62 (2019) 295–308.
[18] Z. Yang, Y. Chen, Z. Le, Y. Ma, GANFuse: a novel multi-exposure image fusion method based on generative adversarial networks, Neural Comput. Appl. (2020) 1–13.
[19] J. Ma, W. Yu, P. Liang, C. Li, J. Jiang, Fusiongan: a generative adversarial network for infrared and visible image fusion, Inf. Fusion 48 (2019) 11–26.
[20] G. Qi, L. Chang, Y. Luo, Y. Chen, Z. Zhu, S. Wang, A precise multi-exposure image fusion method based on low-level features, Sensors 20 (2020) 1597.
[21] W.-R. Sie, C.-T. Hsu, Alignment-free exposure fusion of image pairs, in: IEEE Int. Conf. Image Process., IEEE, 2014, pp. 1802–1806.
[22] S. Wold, K. Esbensen, P. Geladi, Principal component analysis, Chemom. Intell. Lab. Syst. 2 (1–3) (1987) 37–52.
[23] S. Li, X. Kang, L. Fang, J. Hu, H. Yin, Pixel-level image fusion: a survey of the state of the art, Inf. Fusion 33 (2017) 100–112.
[24] N.D. Bruce, J.K. Tsotsos, Saliency, attention, and visual search: an information theoretic approach, J. Vis. 9 (3) (2009) 5.
[25] A.M. Treisman, G. Gelade, A feature-integration theory of attention, Cogn. Psychol. 12 (1) (1980) 97–136.
[26] X. Hou, J. Harel, C. Koch, Image signature: highlighting sparse salient regions, IEEE Trans. Pattern Anal. Mach. Intell. 34 (1) (2011) 194–201.
[27] K. He, J. Sun, X. Tang, Guided image filtering, in: Eur. Conf. Comput. Vision, 2010, pp. 1–14.
[28] P.J. Burt, R.J. Kolczynski, Enhanced image capture through fusion, in: Int. Conf. Comput. Vision, 1993, pp. 173–182.
[29] K. Ma, Z. Duanmu, H. Yeganeh, Z. Wang, Multi-exposure image fusion by optimizing a structural similarity index, IEEE Trans. Comput. Imaging 4 (1) (2017) 60–72.
[30] I. Merianos, N. Mitianoudis, Multiple-exposure image fusion for HDR image synthesis using learned analysis transformations, J. Imaging 5 (3) (2019) 32.
[31] Y. Fang, H. Zhu, K. Ma, Z. Wang, S. Li, Perceptual evaluation for multi-exposure image fusion of dynamic scenes, IEEE Trans. Image Process. 29 (2019) 1127–1138.
[32] K. Ma, K. Zeng, Z. Wang, Perceptual quality assessment for multi-exposure image fusion, IEEE Trans. Image Process. 24 (11) (2015) 3345–3356.
[33] A. Mittal, R. Soundararajan, A.C. Bovik, Making a "completely blind" image quality analyzer, IEEE Signal Process. Lett. 20 (3) (2012) 209–212.
[34] A. Mittal, A.K. Moorthy, A.C. Bovik, No-reference image quality assessment in the spatial domain, IEEE Trans. Image Process. 21 (12) (2012) 4695–4708.
[35] A. Mittal, A.K. Moorthy, A.C. Bovik, Blind/referenceless image spatial quality evaluator, in: Conf. Signals Syst. Comput., 2011, pp. 723–727.

[36] N. Venkatanath, D. Praneeth, M.C. Bh, S.S. Channappayya, S.S. Medasani, Blind image quality evaluation using perception based features, in: Nat. Conf. Commun., 2015, pp. 1–6.
[37] H. Sheikh, Live image quality assessment database release 2, Accessed March 09, 2021, http://live.ece.utexas.edu/research/quality.
[38] Z. Wang, A.C. Bovik, H.R. Sheikh, E.P. Simoncelli, Image quality assessment: from error visibility to structural similarity, IEEE Trans. Image Process. 13 (4) (2004) 600–612.
[39] Y. Xu, Z. Li, W. Chen, C. Wen, Color mapping functions for HDR panorama imaging: weighted histogram averaging, arXiv preprint arXiv:2111.07283 (2021).
[40] J. Ma, Y. Ma, C. Li, Infrared and visible image fusion methods and applications: a survey, Inf. Fusion 45 (2019) 153–178.
[41] Y. Liu, X. Chen, J. Cheng, H. Peng, Z. Wang, Infrared and visible image fusion with convolutional neural networks, Int. J. Wavelets Multiresolution Inf. Process. 16 (03) (2018) 1850018.
[42] H. Li, X.-j. Wu, T.S. Durrani, Infrared and visible image fusion with ResNet and zero-phase component analysis, Infrared Phys. Technol. 102 (2019) 103039.
[43] D.P. Bavirisetti, G. Xiao, J. Zhao, R. Dhuli, G. Liu, Multi-scale guided image and video fusion: a fast and efficient approach, Circuits Syst. Signal Process. 38 (12) (2019) 5576–5605.
[44] X. Zhang, P. Ye, G. Xiao, Vifb: a visible and infrared image fusion benchmark, in: IEEE Conf. Comput. Vision Pattern Recognit. Workshops, 2020.
[45] H.R. Sheikh, A.C. Bovik, Image information and visual quality, IEEE Trans. Image Process. 15 (2) (2006) 430–444.